

C@SnS₂ core-shell 0D/2D nanocomposite with excellent electrochemical performance as lithium-ion battery anode

Changqing Jin^{1*}, Yongxing Wei¹, Ruihua Nan¹, Zengyun Jian¹, Qingping Ding^{2*}

¹Shaanxi Key Laboratory of Optoelectronic Functional Materials and Devices, School of Materials and Chemical Engineering, Xi'an Technological University, Xi'an 710021, People's Republic of China. E-mail: eaglejin@xatu.edu.cn;

²Ames National Laboratory, U.S. DOE, and Department of Physics and Astronomy, Iowa State University, Ames, Iowa 50011, USA. E-mail: qpding@ameslab.gov

Abstract: C@SnS₂ core-shell 0D/2D nanocomposite was successfully prepared by a one-step hydrothermal method. The SnS₂ nanosheets were heterogeneously nucleated and grown on the surface of carbon spheres. As an anode for lithium-ion batteries, the electrochemical performance of the C@SnS₂ composite outperforms that of SnS₂ nanoflowers. After 100 cycles, the reversible discharge specific capacity reaches an impressive value of 802 mAh g⁻¹ at a current density of 100 mA g⁻¹. Even after 600 cycles, the discharge specific capacity remains a value of 442 mAh g⁻¹, under a high current density of 1 A g⁻¹. This remarkable lithium-ion storage performance can be attributed to the unique core-shell nanostructure and the synergy between SnS₂ nanosheets and carbon spheres. This study advances our understanding of the vital role of carbon in fabricating nano-heterojunction or composite electrodes and provides a feasible route to significantly improve the electrochemical properties of SnS₂ and other metal sulfides.

Key word: Lithium-ion battery; Anode material; SnS₂; heterojunction; carbon

1. Introduction

SnS_2 is an attractive candidate for lithium-ion battery anodes due to its high theoretical specific capacity (645 mAh g^{-1}), low cost, low toxicity, easy production, unique conversion reaction and alloying lithium storage mechanism [1-3]. However, it suffers from poor conductivity and volume expansion during charge and discharge processes, leading to limitations in rate performance and cycle stability [4-7]. To overcome these challenges, two key strategies have been proposed.

The first approach involves the synthesis of nanostructured SnS_2 materials with varying microstructures and morphologies [8,9], such as 0D nanoparticles, 1D nanotubes, 2D nanosheets [10-12], and 3D nanoflowers [13]. Compared to bulk SnS_2 , nanostructured SnS_2 materials offer several advantages in terms of improving lithium storage performance. They effectively alleviate volume expansion, provide a larger specific surface area for enhanced Li storage, facilitate electrolyte infiltration, and promote lithium ion diffusion, thereby enhancing kinetic performance during electrochemical reactions.

The second approach focuses on combining SnS_2 with a support material that exhibits excellent conductivity, stable crystal structure, and minimal volume expansion during lithium intercalation [14-19]. For instance, the combination of nanostructured SnS_2 with carbon-based materials, including graphene, carbon nanotubes, and mesoporous carbon, has shown significant improvements in lithium storage performance [15-19]. Liu et al. [16] fabricated flower-like SnS_2 nanosheets uniformly anchored in the pores of a carbon membrane using a hydrothermal method

and annealing treatment, achieving a reversible capacity of 808.9 mAh g⁻¹ for LIBs at 50 mA g⁻¹. Likewise, Cheng et al. [17] synthesized SnS₂/CNTs composites via a hydrothermal method and in-situ vulcanization technique, obtaining a reversible capacity of 660 mAh g⁻¹ after 100 cycles at a current density of 0.1 A g⁻¹. The introduction of carbon materials helps alleviate volume changes caused by deintercalation/intercalation of Li⁺ ions, accelerates lithium ion and electron kinetics, and improves overall conductivity of the composites.

However, the complexity and high cost associated with the preparation of these samples hinder their large-scale applications. Therefore, developing a scalable and straightforward synthesis method for SnS₂ matrix composites, particularly SnS₂ and carbon composites, is crucial. In this study, we successfully prepared a C@SnS₂ core-shell 0D/2D nanocomposite using a one-step hydrothermal method. We employed C45 as nucleating agents to achieve heterogeneous nucleation and growth of SnS₂, inhibiting the agglomeration of SnS₂ nanomaterials. Furthermore, carbon spheres improved the conductivity of the nanocomposite and alleviate volume expansion caused by deintercalation/intercalation of Li⁺ ions.

2. Experimental part

2.1 Preparation of C@SnS₂ composite and SnS₂

C@SnS₂ core-shell 0D/2D nanocomposite was synthesized using a one-step hydrothermal method. The procedure involved several steps: (1) Mixing 0.4 g of tin tetrachloride pentahydrate (SnCl₄ • 5H₂O) and 0.3 g of thioacetamide (TAA) in anhydrous ethanol to form a transparent solution. (2) Adding 0.1 g of acetylene

carbon black (C45) to the solution and sonicating it for 30 minutes at room temperature. (3) Transferring the suspension to a 100 mL hydrothermal reaction vessel and performing solvothermal processing at 180 °C for 12 hours. (4) Collecting the resulting black C@SnS₂ nanocomposite through centrifugation, followed by thorough washing with water and alcohol, each for three times. Finally, the nanocomposite was dried in vacuum at 60 °C for 12 hours.

The preparation process for SnS₂ nanoflowers was similar to that of the C@SnS₂ nanocomposite, except that C45 was not included in the raw materials.

2.2 Materials Characterization

The crystal structures of the samples were analyzed using X-ray diffraction (D2 PHASER Gen2) with Cu K α radiation in the 2 θ range of 15-80°. Raman scattering spectra of SnS₂ and C@SnS₂ samples were obtained using a Renishaw spectrophotometer with a 532 nm Horiba HR evolution laser. X-ray photoelectron spectroscopy (XPS) spectra were collected using an imaging photoelectron spectrometer (Thermo ESCALAB 250XI). The microstructures and morphologies of SnS₂ and C@SnS₂ materials were examined by using transmission electron microscopy (TEM, JEM-2010) and scanning electron microscopy (HR-SEM, Hitachi, S-4800). Energy-dispersive spectroscopy (EDS) was employed to investigate the element distribution.

2.3 Electrochemical Measurements

Coin cells (2032) were assembled in a glovebox with O₂ and H₂O concentrations below 0.1 ppm to measure the electrochemical performance of the working electrode.

The slurry was prepared by mixing C@SnS₂ (70 wt.%), acetylene black (20 wt.%), and Carboxymethyl cellulose (CMC, 10 wt.%) with water. The resulting slurry was coated onto a copper foil using an automatic coating machine and then dried in a vacuum oven at 80 °C for 12 hours. The mass loading amount of active material was about 0.3 mg cm⁻². Finally, the coated electrode was transferred to a vacuum glovebox under an Ar atmosphere. The lithium foil served as the counter electrode, and a Celgard 2500 membrane was used as the separator. The electrolyte consisted of a 1 M LiPF₆ dissolved in a mixture of ethylene carbonate (EC)/dimethyl carbonate (DMC)/ethyl methyl carbonate (EMC) (1:1:1 vol%). The assembled CR2032 button-cell battery was subjected to constant current charge and discharge tests using a Xinwei tester ct-4008 produced by Newell Electronics. The voltage range for the charge/discharge test was set at 0.01-3 V. Cyclic voltammetry (CV) measurements were performed using a CHI660E electrochemical workstation within a voltage range of 0.01-3 V. Electrochemical impedance spectroscopy (EIS) was conducted using the same instrument, with a frequency range from 0.01 Hz to 10 kHz and a perturbation voltage of 0.005 V.

3. Results and discussion

Figure 1a shows the XRD diffraction patterns of SnS₂ nanoflowers and C@SnS₂ nanocomposites. The diffraction peaks of both samples are consistent with the hexagonal SnS₂ (JCPDS NO. 23-0677). No additional diffraction peaks were observed, indicating the high qualities of the samples. Notably, no diffraction peaks from C45 were observed. This is probably because the carbon content in the samples

is very low, making it difficult for XRD to detect.

Raman spectra of SnS₂ and C@SnS₂ composites are shown in Figure 1b. In the Raman spectrum of pure SnS₂, a distinct peak appears at 320 cm⁻¹, corresponding to the A_{1g} mode of SnS₂ vibrating in the sulfur-tin-sulfur plane [20]. In the case of C@SnS₂ composites, in addition to the SnS₂ peak at 320 cm⁻¹, two additional Raman peaks appear at 1344 cm⁻¹ and 1585 cm⁻¹. These two peaks can be attributed to the D-band and G-band of carbon materials [21-23], providing evidence for the presence of C45 in the composites.

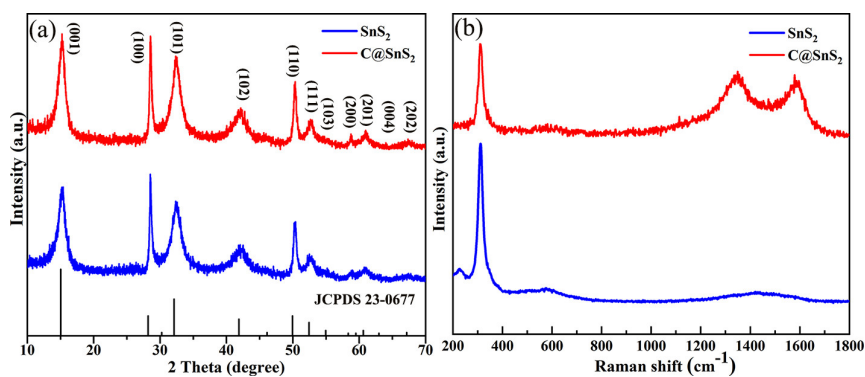


Fig. 1 XRD patterns (a) and Raman spectra (b) of the samples.

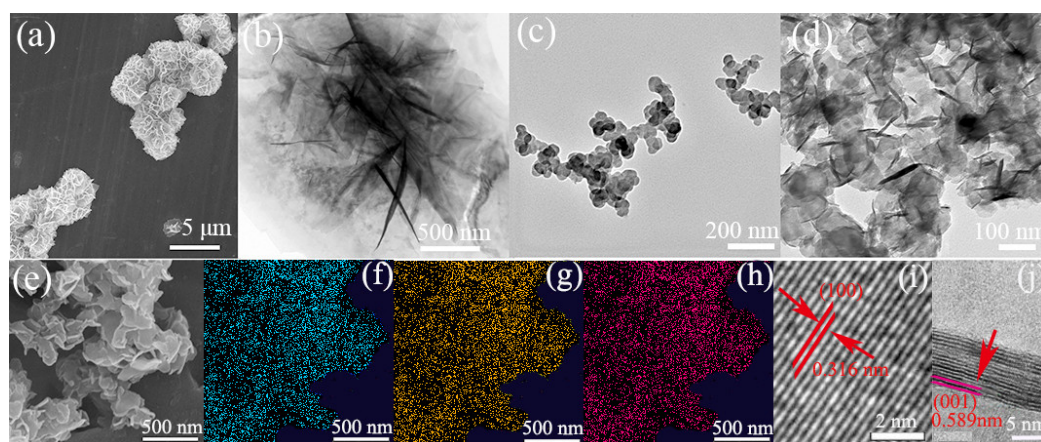


Fig. 2 The morphologies, microstructures and chemical compositions of the samples. SEM image of the SnS₂ nanoflowers (a); TEM image of the SnS₂ nanoflowers (b); TEM image of C45 (c); TEM image of the C@SnS₂ composites (d); SEM image (e), and corresponding elemental mapping of C (f), S (g), and Sn (h) of the C@SnS₂ composites; HRTEM images of the SnS₂

nanoflowers (i); and C@SnS₂ composites (j).

The morphologies, microstructures and chemical compositions of the C@SnS₂ core-shell nanocomposite and SnS₂ nanoflowers were examined by using SEM, TEM and EDS, as shown in Figure 2. Figure 2a reveals the hierarchical structure of self-assembled SnS₂ nanoflowers composed of nanosheets, with an overall size of approximately 3 μm. Figure 2b demonstrates that the nanosheets have a thickness of tens of nanometers. In Figure 2c, uniform carbon spheres with a diameter of around 70 nm can be observed, and their surfaces appear smooth. These carbon spheres come together to form a conductive skeleton. Figure 2d depicts the C@SnS₂ core-shell nanocomposite consisting of cored carbon nanospheres and shelled SnS₂ nanosheets. The original carbon sphere skeleton is preserved, and the SnS₂ nanosheets are distributed on its surface. This suggests that when carbon spheres are used as nucleating agents, SnS₂ nanosheets no longer self-assemble into nanoflowers but instead undergo heterogeneous nucleation and grow on the surface of the carbon spheres. Figure 2e also shows that carbon nanoparticles are evenly distributed among the nanosheets. These are consistent with the results of the TEM (Figure 2d). Figures 2f-h show the elemental mapping of C@SnS₂ nanocomposites (corresponding to Figure 2e), which suggests a uniform distribution of C, Sn, and S. This further confirms the formation of a uniform C/SnS₂ nanocomposites with core-shell structure. Figure 2i indicates that the well-resolved interplanar spacing of lattice fringe is about 0.316 nm, which corresponds to the (100) plane of SnS₂. In Figure 2j, the lattice fringe with a lattice spacing of about 0.589 nm can be assigned to the (001) plane of SnS₂.

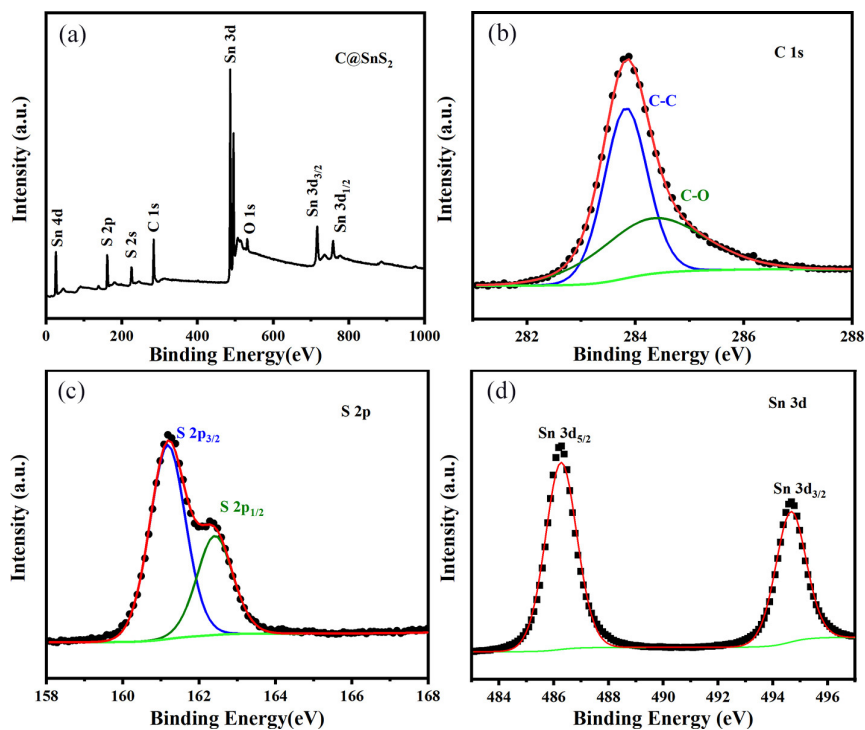


Fig. 3 XPS spectra of C@SnS₂ (a); high resolution C 1s (b), S 2p (c) and Sn 3d (d) peaks.

XPS was employed to examine the surface characteristics and chemical composition of the C@SnS₂ core-shell nanocomposite, as shown in figure 3. Figure 3a presents the XPS spectrum, which exhibits distinct peaks corresponding to Sn, S, and C, confirming the high purity of the synthesized samples. The presence of oxygen (O) may be attributed to the adsorption of oxygen on the sample surface. High-resolution spectra of the C 1s, S 2p, and Sn 2p regions are illustrated in figures 3b-d, respectively. In figure 3b, Gaussian fits of the C 1s peak within the energy range of 281-288 eV are depicted. The peaks at 283.9 and 284.5 eV can be assigned to C-C and C-O bonds, respectively, indicating the existence of carbon [24]. Figure 3c displays the S 2p spectrum of C@SnS₂, showing two distinct peaks after deconvolution at binding energies of 161.2 and 162.6 eV. These peaks correspond to S 2p_{3/2} and S 2p_{1/2}, respectively, confirming the presence of S²⁻ in the composite [25].

Furthermore, figure 3d provides the detailed spectra of Sn 3d, revealing two symmetric peaks observed at binding energies of 486.3 and 494.7 eV. These peaks correspond to Sn 3d_{5/2} and Sn 3d_{3/2}, respectively [26], confirming the presence of Sn⁴⁺ in the SnS₂ component of the composite.

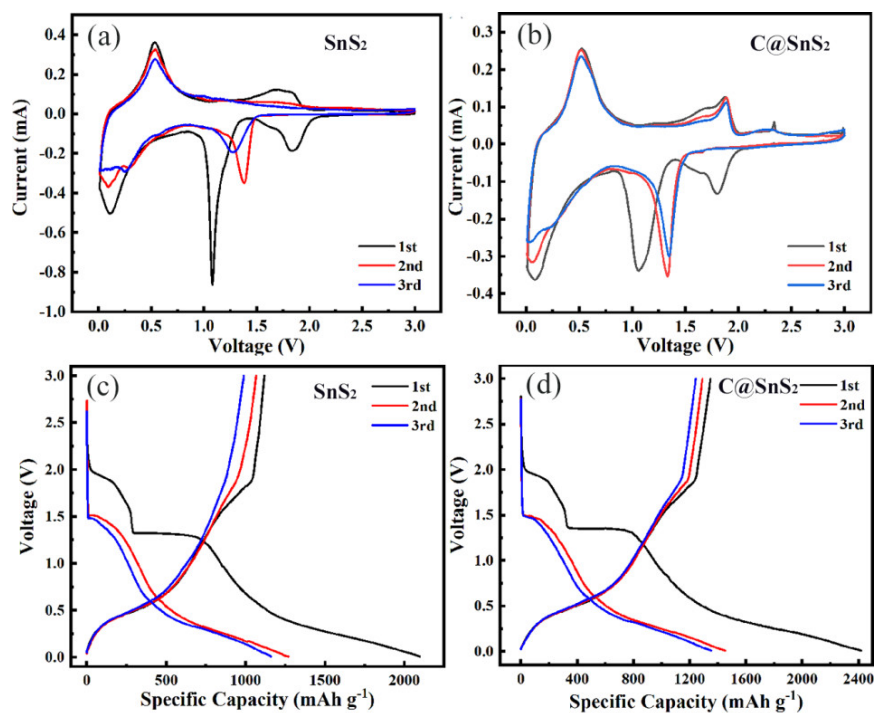


Fig. 4 CV curves of SnS₂ nanoflower (a) and C@SnS₂ nanocomposite (b); discharge-charge profiles at 100 mA g⁻¹ of SnS₂ nanoflower (c) and C@SnS₂ nanocomposite (d).

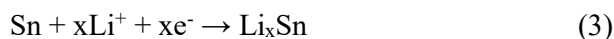
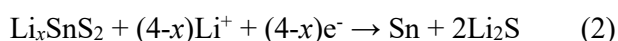
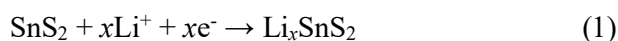
The CV curves of SnS₂ nanoflowers and C@SnS₂ nanocomposite nanoflowers were obtained with a scanning rate of 0.1 mV/s, as depicted in figures 4a and 4b, respectively.

For SnS₂ nanoflowers, three reduction peaks were observed during the first cathodic scanning cycle (Figure 4a). The peak at approximately 1.82 V corresponds mainly to the formation of Li_xSnS₂ (equation 1). However, this peak disappears in subsequent scanning cycles, indicating its irreversibility. The peak at around 1.08 V

can be attributed to the decomposition of Li_xSnS_2 , the formation of Sn and Li_2S (equation 2) and the formation of solid electrolyte interphase (SEI) [5, 27, 28]. The weak and broad reduction peak at about 0.57 V can be assigned to the insertion of Li^+ into tin metal and the formation of Li_xSn alloy [28] (equation 3). During the first anodic scan, two oxidation peaks are observed during the first anodic scanning cycle. The peak at approximately 0.53 V is attributed to the delithiation reaction of Li_xSn , forming metallic Sn. The peak at around 1.75 V may be related to the conversion of metallic Sn to SnS_2 [29]. As the cycling progresses, the enclosed area of the CV curve gradually decreases, and the specific capacity of SnS_2 continuously decreases, indicating poor reversibility. This phenomenon is due to the significant volume change of the material during charge and discharge, resulting in a continuous decline in the anode capacity.

In the case of the C@SnS_2 composite (figure 4b), the reaction mechanism for the three reduction peaks at approximately 1.82 V, 1.08 V, and 0.65 V is similar to that of SnS_2 during the initial discharge cycle. During the first anodic scan, an additional anodic peak at 2.34 V, which is not yet observed during the subsequent cycles, is attributed to the lithium deintercalation of the SnS_2 layers without causing phase decomposition (equation 1) [2,20,28]. The anodic peak located at 1.9 V is also associated with the continuous extrusion of lithium ions from SnS_2 without phase decomposition [28-31]. The oxidation peaks at around 0.54 V and 1.65 V correspond to the dealloying reaction of Li_xSn and the conversion of metallic Sn to SnS_2 during the first charging cycle, respectively. Compared to SnS_2 nanoflowers, the oxidation

peak at approximately 1.9 V in subsequent cycles for the C@SnS₂ composite exhibits higher sharpness and coincidence, indicating improved reversibility of the conversion reaction to some extent. Moreover, although the CV curve of the C@SnS₂ composite shows a similar shape to that of pure SnS₂, the high coincidence degree indicates better reversibility and electrochemical stability for the C@SnS₂ composite.



Comparing the CV curves of SnS₂ nanoflower and C@SnS₂ nanocomposite, it can be found that the positions of their oxidation and reduction peaks are almost the same, indicating that their lithium storage mechanisms are also the same. The only difference is the anodic peak at 2.34 V of C@SnS₂ nanocomposite, which is a typical feature of interlayer delithiation of layered SnS₂ without causing a change in crystal structure.

The discharge/charge curves of the samples are shown in figures 4c and 4d. In the first cycle of these curves, three distinct discharging voltage platforms (approximately 1.9 V, 1.34 V, and 0.5 V) and two charging voltage platforms (around 0.5 V and 1.75 V) can be observed. These platforms correspond to the three reduction peaks and two oxidation peaks found in the CV curve analysis. Specifically, the three discharging voltage platforms are associated with the following processes: lithium intercalation reaction (1.9 V), conversion reaction as well as the formation of SEI (1.34 V), and the alloying reaction of Sn (0.5 V). The two charging voltage platforms

correspond to the dealloying of Li_xSn (0.5 V) and the conversion of Sn to SnS_2 (1.75 V). These observations align consistently with the results obtained from the corresponding CV curve analysis.

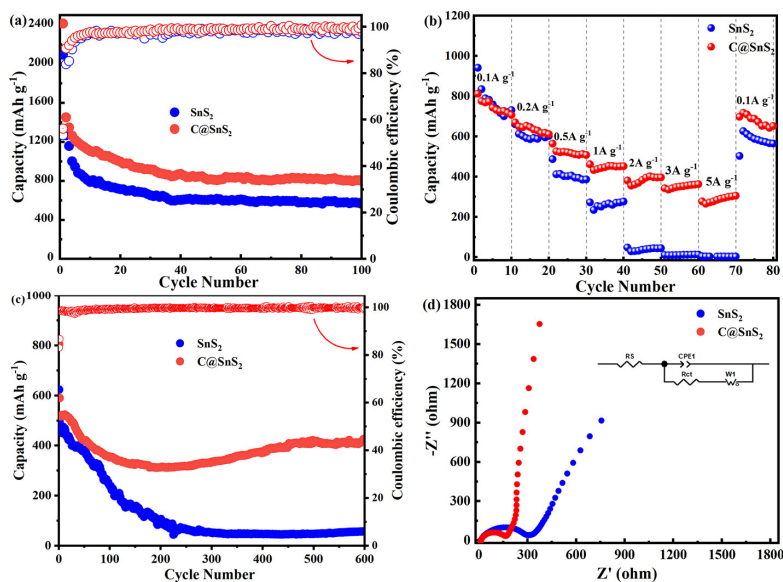


Fig. 5 Cycling performance at 100 mA g^{-1} (a), rate capability (b), long-term cycling performance at 1 A g^{-1} (c), and EIS spectra (d) of the samples.

The cyclic performance curve of the samples at a current density of 100 mA g^{-1} is presented in figure 5a. The specific discharge capacity of the C@SnS_2 composite initially experiences a rapid decrease in the first few cycles, primarily attributed to the formation of a solid electrolyte interphase (SEI) film and electrolyte side reactions. Subsequently, the capacity gradually decreases at a slower rate, and eventually stabilizes after 35 cycles. After 100 cycles, the specific discharge capacity of the C@SnS_2 composite reaches 802 mAh g^{-1} . In comparison, the SnS_2 nanoflower electrode achieves a specific discharge capacity of 565 mAh g^{-1} after 100 cycles. It is evident that the specific capacity of the C@SnS_2 composite is significantly higher than that of pure SnS_2 .

In summary, the C@SnS₂ composite investigated in this study demonstrates favorable electrochemical properties compared with other SnS₂ based materials, as summarized in Table 1.

Table 1. The comparison of LIB electrochemical performances for different SnS₂ composites

sample	Current density (mA g ⁻¹)	cycle	Specific capacity (mAh g ⁻¹)	reference
SnS ₂	200	100	548	[20]
SnS ₂	100	100	549	[2]
CPN@ SnS ₂	60	100	699	[7]
SnS ₂ /CP	200	60	2073.8	[11]
SnS ₂ /SnO ₂ @C/rGO	783	300	689	[12]
SnS ₂ NP/GNs	100	150	600	[32]
SnS ₂ -graphene	129	30	570	[33]
SnS ₂ -CM	200	200	320	[14]
MC- SnS ₂ NSs	100	50	429	[34]
SnS ₂ @RGO	117	60	564	[35]
SnS ₂ /G	48	100	735	[15]
C@ SnS ₂	100	100	802	This work

Figure 5b displays the rate performance curves of the samples at various current densities, namely 0.1, 0.2, 0.5, 1.0, 2.0, 3.0, and 5.0 A g⁻¹. The specific discharge capacities of the C@SnS₂ composite are 774, 646, 517, 453, 395, 353, and 291 mAh g⁻¹, respectively. In comparison, the corresponding capacities for SnS₂ nanoflowers are 725, 592, 406, 260, 37, 11, and 4 mAh g⁻¹, respectively. Upon returning to a current density of 0.1 A g⁻¹, the specific discharge capacities for the C@SnS₂ composite and SnS₂ nanoflowers are 688 mAh g⁻¹ and 583 mAh g⁻¹, respectively. The capacity retention rates are 88.86% for the C@SnS₂ composite and 80.36% for SnS₂ nanoflowers. Importantly, as the current density increases, a wider gap in specific capacity between SnS₂ nanoflowers and the C@SnS₂ composite becomes apparent. At

2 A g⁻¹, the maximum gap reaches 358 mAh g⁻¹, and even at 5 A g⁻¹, the gap remains as high as 287 mAh g⁻¹. Clearly, the rate performance of the C@SnS₂ composite surpasses that of SnS₂ nanoflowers, particularly at high current densities.

Figure 5c shows the long cycle life of SnS₂ nanoflowers and the C@SnS₂ composite at 1 A g⁻¹. For the C@SnS₂ composite, the capacity gradually declines to a minimum of 313 mAh g⁻¹ within the first 200 cycles. Subsequently, the capacity begins to recover and eventually stabilizes. After 600 cycles, the specific discharge capacity reaches 442 mAh g⁻¹. As for SnS₂ nanoflowers, the specific discharge capacity gradually decreases during the initial 250 cycles and then stabilizes. After 600 cycles, the capacity is 58 mAh g⁻¹. The exceptional performance of the C@SnS₂ composite is primarily attributed to the synergistic effect between carbon and SnS₂, which enhances the reversibility and electrochemical performance of the conversion reaction [36]. The C@SnS₂ composite undergoes an initial period of decreasing capacity followed by recovery, mainly due to electrode activation throughout the cycling process [37].

Figure 5d presents the EIS spectrum of the samples before cycling. The equivalent circuit diagram of the electrodes illustrates the components, as shown in Fig. 5d. R_s represents the internal ohmic resistance of the battery, encompassing the resistance of both the electrode and electrolyte. R_{ct} indicates the charge transfer resistance in the electrochemical reaction, while W₁ represents the Warburg impedance resulting from lithium ion diffusion in the solid phase [34, 38]. The EIS curves consist of a semicircular arc and an oblique line. The semicircular arc at

medium and high frequencies represents R_{ct} , whereas the oblique line in the low-frequency region represents W_1 of lithium ions diffusing in the solid phase. It is evident that the charge transfer resistance of the $C@SnS_2$ composite is lower than that of SnS_2 nanoflowers. This reduced R_{ct} effectively improves electronic conductivity and electrochemical properties, which aligns with the conclusions regarding rate performance.

The remarkable high capacity and excellent cycle stability of the $C@SnS_2$ composite can be primarily attributed to the synergistic effect between the SnS_2 nanosheets and carbon spheres. This synergy enhances the reversibility and electrochemical properties of the conversion reaction. Additionally, the unique core-shell structure prevents agglomeration of the SnS_2 nanosheets. Furthermore, the presence of carbon spheres not only mitigates volume changes during lithium deintercalation/intercalation but also accelerates electron transfer kinetics. These factors collectively contribute to the improved conductivity and electrode stability over cycling [5, 30, 31].

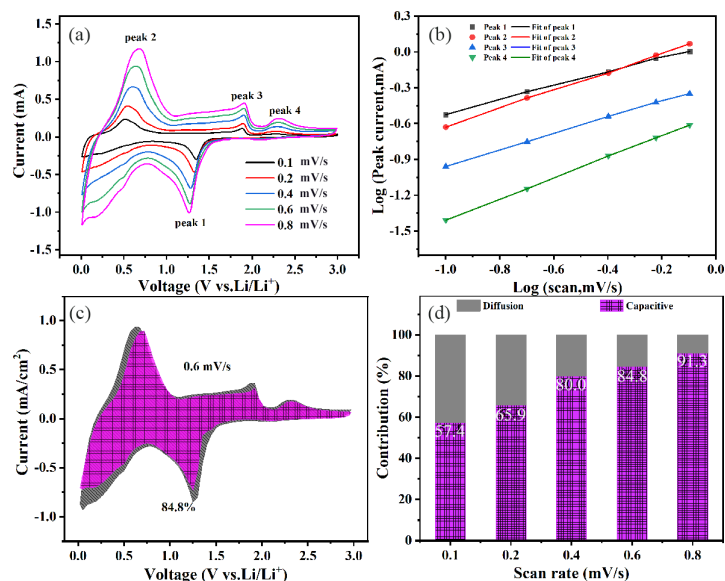


Fig. 6 (a) CV curves of C@SnS₂ at various scan rates in range of 0.1–0.8 mV/s, (b) linear fitting relationship of log(*i*) vs. log(*v*), (c) the pictorial estimation of pseudocapacitive for C@SnS₂ at a scan rate of 0.6 mV/s, (d) contribution of pseudocapacitive and diffusion-controlled effect of C@SnS₂ at various scan rates in range of 0.1–0.8mV/s.

To further investigate the electrochemical kinetics and energy storage mechanism, CV curves of the C@SnS₂ composites were measured at various scan rates (Fig. 6a). The enclosed area within the CV curve represents the total capacity, comprising contributions from both the diffusion and the pseudo capacitance. As the scanning rate increases, the peak positions of the cathodic and anodic peaks shift towards their respective directions, indicating enhanced electrode polarization [39]. To assess the relative proportions of pseudocapacitive and diffusion contributions, logarithmic current-voltage plots based on equations (4) and (5) were generated (Fig. 6b). The current value in the CV curve, at a specific scan rate and potential, can be regarded as the sum of the diffusion current i_{diff} and capacitive current i_{cap} . The slower diffusion process is responsible for i_{diff} , while i_{cap} arises from the pseudocapacitive behavior occurring at the surface of the electrode material.

$$i = i_{\text{diff}} + i_{\text{cap}} = a\nu^b \quad (0.5 \leq b \leq 1) \quad (4)$$

$$\log i = b \log \nu + \log a \quad (5)$$

Where ν is the scanning rate and i is the response current. a and b are variable parameters, which can be obtained from the intercept and slope of logarithmic current-voltage plots. b value represents the dynamic properties of electrode materials. $b = 1$ indicates that the current is all attributed to the capacitive behavior, $i(\nu) = i_{\text{cap}}$; and $b = 0.5$ indicates that the current is all diffusion process, $i(\nu) = i_{\text{diff}}$. The value of b is between 0.5 and 1, this indicates both contributions exist. By linear fitting, the b values of reduction peaks 1 and 2 are 0.59 and 0.77, while the b values of reduction peaks 3 and 4 are 0.68 and 0.88, the C@SnS₂ composite has both capacitive lithium storage behavior and diffusion lithium storage behavior, and is more inclined to capacitive lithium storage.

$$i/\nu^{1/2} = k_1\nu^{1/2} + k_2 \quad (i = k_1\nu + k_2 \nu^{1/2}) \quad (6)$$

$k_1\nu$ is the capacitance contribution and $k_2 \nu^{1/2}$ is the diffusion contribution. Using formula (6), we analyze the pseudocapacitive distribution at different scanning speeds. At 0.6 mV/s, the pseudocapacitive contribution reaches 84.8% (Fig. 6c). The pseudocapacitive contribution at different scanning rates is also quantified (Fig. 6d). The pseudocapacitive contribution increases with the increase of scanning rate. At a high scan rate of 0.8 mV/s, the pseudocapacitive contribution of C@SnS₂ is 91.3%, which is 1.59 times as that at a low scan rate of 0.1 mV/s. Compared with SnS₂ nanoflower, C@SnS₂ nanocomposite has better lithium storage performance. It can be concluded that the excellent lithium storage performance of C@SnS₂ nanocomposite

comes from the higher pseudo capacitance contribution, which has also been observed in other SnS₂-based nanocomposites [40, 41].

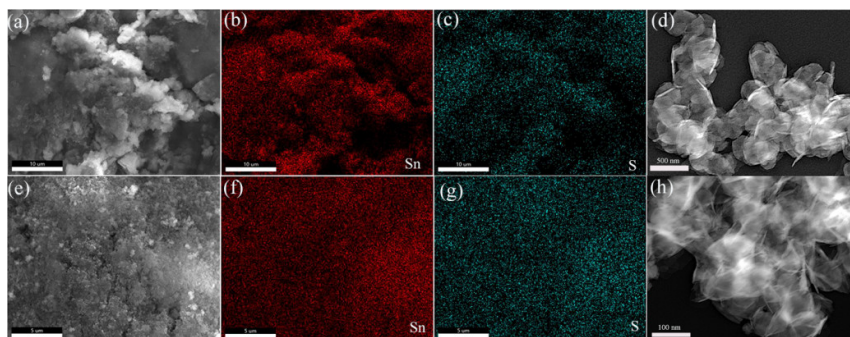


Fig. 7 SEM image (a), and corresponding elemental mapping of Sn (b), S (c) of SnS₂ nanoflowers electrode after 100 cycles at a current density of 1 A g⁻¹; TEM image of SnS₂ nanoflowers (d) after 100 cycles at a current density of 1 A g⁻¹; SEM image (e), and corresponding elemental mapping of Sn (f), S (g) of C@SnS₂ composites electrode after 100 cycles at a current density of 1A g⁻¹; TEM images of C@SnS₂ composites (h) after 100 cycles at a current density of 1 A g⁻¹.

In order to further understand the stability of the electrochemical lithium storage performance of SnS₂ nanoflowers and C@SnS₂ nanocomposite, the morphology, composition, and microstructure characteristics of the materials after 100 cycles are revealed in Figure 7. Figure 7a shows that the SnS₂ nanoflowers electrode exhibits significant surface roughness, collapse, and cracks after cycling. The elemental mapping of SnS₂ nanoflowers (corresponding to Figure 7a) in Figures 7b-c confirmed that the homogeneity of components was also affected to a certain extent. Figure 7d shows (The electrode material was alternately cleaned with deionized water and alcohol multiple times) that the microstructure of SnS₂ nanoflowers has collapsed into irregular nanosheets. Figure 7e shows that the C@SnS₂ nanocomposite electrode exhibits few cracks and smooth surface structure after cycling. The elemental mapping of SnS₂ nanoflowers (corresponding to Figure 7e) in Figures 7f-g confirmed

that the homogeneity of components has been highly preserved. Figure 7h confirms the high stability of the microstructure of C@SnS₂ nanocomposite. In a word, compared with SnS₂ nanoflowers, the composition uniformity, microstructure integrity, and surface smoothness of C@SnS₂ nanocomposite electrodes are better after cycling. This may partly explain why the electrochemical lithium storage performance of C@SnS₂ nanocomposite is much better than that of SnS₂ nanoflowers.

4. Conclusion

C@SnS₂ nanocomposite was successfully prepared by a simple one-step hydrothermal method. SnS₂ nanosheets were heterogeneous nucleated and grown on the surface of carbon spheres. As an anode material of LIBs, the electrochemical performance of C@SnS₂ composite is much better than that of SnS₂ nanoflowers. This is due to the synergistic effect of carbon nanoparticles and SnS₂ nanosheets, which is inherent in the unique 0D/2D core-shell structure. On the one hand, carbon spheres not only effectively adsorb polysulfides to prevent the shuttle effect, but also facilitate the charge transfer in the process of discharge/charge and prevent the aggregation of SnS₂ nanosheets. In addition, carbon spheres can effectively alleviate the volume expansion during lithium intercalation. On the other hand, C@SnS₂ composite has obvious pseudo capacitance behavior. The excellent performance makes C@SnS₂ core-shell 0D/2D nanocomposite a good candidate of LIBs anode materials, especially in rapid charge/discharge and power energy applications. This core-shell 0D/2D architectural design and simple synthesis method can be extended to the synthesis of other metal sulfides, which provides more options for improving

performance of the anode of metal sulfide LIBs.

CRedit authorship contribution statement

Changqing Jin: Supervision, Conceptualization, Writing – original draft, Yongxing

Wei: Visualization, Software, Ruihua Nan: Investigation, Validation, Zengyun Jian:

Writing– review & editing, Qingping Ding: Writing – review & editing, Investigation.

Declaration of competing interest

The authors declare that they have no known competing financial interests or personal relationships that could have appeared to influence the work reported in this paper.

Acknowledgement

This work was supported by the National Natural Science Foundation of China (Grant Project Nos. 11404251 and 11704301), the Natural Science Basic Research Plan in Shaanxi Province (Program Nos. 2019JM414 and 2018JQ1092). The work at Ames National Laboratory was supported by the U.S. Department of Energy, Division of Materials Sciences and Engineering. Ames National Laboratory is operated for the U.S. Department of Energy by Iowa State University under Contract No. DE-AC02-07CH11358.

References

- [1] K. Chang, W. Zhen, G. Huang, L. He, W. Chen, J.Y. Lee **Few-layer SnS₂/graphene hybrid with exceptional electrochemical performance as lithium-ion battery anode** *J. Power Sources*, 201 (2012), pp.259-266
- [2] Q. Wu, L. Jiao, J. Du, J. Yang, L. Guo, Y. Liu, Y. Wang, H. Yuan **One-pot synthesis of**

- three-dimensional SnS₂ hierarchitectures as anode material for lithium-ion batteries** *J. Power Sources*, 239 (2013), pp. 89-93
- [3] J. M. Ma, D. Lei, L. Mei, X. C. Duan, Q.H. Li **Plate-like SnS₂ nanostructures: Hydrothermal preparation, growth mechanism and excellent electrochemical properties** *CrystEngComm*, 14 (2012), pp. 832-836
- [4] H. Chen, B. Zhang, J. Zhang, W. Yu, J. C. Ding, Z. Y. Li, H. M. Lei, S. N. Chen **In-situ grown SnS₂ nanosheets on rGO as an advanced anode material for lithium and sodium ion batteries** *Front. Chem.*, 6 (2018), p. 629
- [5] G. Y. Yu, X. J. Chen, A. S. Wang, Y. L. Wang **Carbon@SnS₂ core-shell microspheres for lithium-ion battery anode materials** *Ionics*, 24 (2018), pp. 2915-2923
- [6] C.X. Zhai, N. Du, H. Zhang, J.X. Yu, D.R. Yang **Multiwalled carbon nanotubes anchored with SnS₂ nanosheets as high-performance anode materials of lithium-ion batteries** *ACS Appl. Mater. Inter.*, 3 (2011), pp. 4067-4074
- [7] X. Chen, Y. Huang, K. Zhang, X. Sheng, M. Wang **Synthesis and high-performance of carbonaceous polypyrrole nanotubes coated with SnS₂ nanosheets anode materials for lithium ion batteries** *Chem. Eng. J.*, 330 (2017), pp. 470-479,
- [8] L. X. Yin, S. M. Chai, J. F. Huang, X. G. Kong and L. M. Pan, **Preparation of hierarchical SnS₂/SnO₂ anode with enhanced electrochemical performances for lithium-ion battery** *Electrochim. Acta*, 238 (2017), pp. 168-177
- [9] A. S. Wang **Preparation of core-shell structure carbon@SnM₂ (M=S, O) microspheres composites and application in lithium-ion batteries** *Int. J. Electrochem. Sci.*, 14 (2019), pp. 3204-3216
- [10] S. Tao, D. J. Wu, S. M. Chen, B. Qian, W. S. Chu, L. Song **A versatile strategy for ultrathin SnS₂ nanosheets confined in a N-doped graphene sheet composite for high performance lithium and sodium-ion batteries** *Chem. Comm.*, 54 (2018), pp. 8379-8382
- [11] Y. Huang, S. Ding, S. Xu, Z. Ma, X. Yuan **Binder-free SnS₂ sheet array with high sulfur vacancy concentration for enhanced lithium storage performance** *Electrochim. Acta*, 409 (2022), p. 139979
- [12] S. Jin, F. Gu, J. Wang, X. Ma, C. Qian, Y. Lan, Q. Han, J. Li, X. Wang, R. Zhang, W. Qiao, L. Ling, M. Jin **Elaborate interface design of SnS₂/SnO₂@C/rGO nanocomposite as a high-performance anode for lithium-ion batteries** *Electrochim. Acta*, 405 (2022), p. 139799
- [13] Y. Chen, H. Liu, X. Guo, S. Zhu, T. Ma **Bimetallic Sulfide SnS₂/FeS₂ nanosheets as high-performance anode materials for Sodium-ion batteries** *ACS Appl. Mater. Inter.*, 13 (2021), pp. 39248-39256
- [14] Y. H. Wang, Y. Y. Zhang, H. Lia, Y. Y. Peng, J. Y. Lia, J. Wang, B. J. Hwang, J. B. Zhao **Realizing high reversible capacity: 3D intertwined CNTs inherently conductive network for CuS as an anode for lithium ion batteries** *Chem. Eng. J.*, 332 (2018), pp. 49-56
- [15] S. Y. Liu, X. Lu, J. Xie, G. S. Cao, X. B. Zhao **Preferential c-axis orientation of ultrathin SnS₂ nanoplates on graphene as high-performance anode for Li-ion batteries** *ACS Appl. Mater. Interfaces.*, 5 (2013), pp. 1588-1595
- [16] H. Liu, C. B. Wei, Z. Q. Ai, M. J. Li, M. Y. Xu, C. Ma, J. L. Shi **The positive effect of 3D interpenetrating network porous structure by carbon membranes on alleviating the volume expansion of SnS₂ nanosheets for enhancing lithium and sodium storage** *Colloid*

- Surface A, 610 (2021), p. 125937
- [17] Y. Y. Cheng, H. Xie, L. Zhou, B. Y. Shi, L. Guo, J. F. Huang **In-situ liquid-phase transformation of SnS₂/CNTs composite from SnO₂/CNTs for high performance lithium-ion battery anode** Appl. Surf. Sci., 566 (2021), p. 150645
- [18] Y. Q. Wu, Y. S. Zhao, W. J. Meng, Y. Xie, J. Zhang, C. J. He, D. L. Zhao **Nanoplates-assembled SnS₂ nanoflowers with carbon coating anchored on reduced graphene oxide for high performance Li-ion batteries** Appl. Surf. Sci., 539 (2021), p. 148283
- [19] M. Cheng, Q. Q. Hu, C. F. Du, J. L. Li, W. H. Liao, J. R. Li, X. Y. Huang **An ionic liquid-assisted route towards SnS₂ nanoparticles anchored on reduced graphene oxide for lithium-ion battery anode** J. Solid. State. Chem., 296 (2021), p. 122022
- [20] A. Q. Zhu, L. L. Qiao, P. F. Tan, Y. J. Ma, Y. Liu, J. Pan **Template-free synthesis of novel SnS₂ array and its superior performances for lithium ion battery** J. Solid. State. Chem., 261 (2018), pp. 16-21
- [21] C.T. Gao, L. Li, A.O. Raji, A. Kovalchuk, Z. W. Peng, H. L. Fei, Y. M. He, N. D. Kim, Q. F. Zhong, E. Xie, J. M. Tour **Tin disulfide nanoplates on Graphene nanoribbons for full Lithium ion batteries** ACS Appl. Mater. Interfaces, 7 (2015), pp. 26549-26556,
- [22] Y. Jiang, Y. B. Guo, W. J. Lu, Z. Y. Feng, B. J. Xi, S. S. Kai, J. H. Zhang, J. K. Feng, S. L. Xiong **Rationally incorporated MoS₂/SnS₂ nanoparticles on Graphene sheets for Lithium-ion and Sodium-ion Batteries** ACS Appl. Mater. Interface, 9 (2017), pp. 27697-27706
- [23] Y. Q. Zhang, Z. L. Ma, D. D. Liu, S. Dou, J. M. Ma, M. Zhang, Z. P. Guo, R. Chen, S.Y. Wang **P-type SnO thin layers on n-type SnS₂ nanosheets with enriched surface defects and embedded charge transfer for lithium ion batteries** J. Mater. Chem. A., 5 (2017), pp. 512-518
- [24] C. J. He, Y. Q. Wang, W. J. Meng, J. Zhang, Y. Xie, Y. L.Hou, D. L. Zhao **Hierarchical micros- pheres constructed by SnS₂ nanosheets and S-doped graphene for high performance lithium /sodium-ion batteries** J. Alloys Compd., 889 (2021), p. 161648
- [25] L. X. Yin, R. L. Cheng, Q. Song, J. Yang, X. G. Kong, J. F. Huang, Y. Lin, H. B. Ouyang **Construction of nanoflower SnS₂ anchored on g-C₃N₄ nanosheets composite as highly efficient anode for lithium ion batteries** Electrochim. Acta, 293 (2019), pp. 408-418
- [26] X. Z. Jin, H. H. Hao, A. M. Wu, G. Song, M. K. Lei, J. J. Zhao, X. X. Gao, G. Z. Cao **Inverse capacity growth and pocket effect in SnS₂ semifilled carbon nanotube anode** ACS Nano, 12 (2018), pp. 8037-8047
- [27] M. S. Balogun, W.T. Qiu, J. H. Jian, Y. C. Huang, Y. Luo, H. Yang, C. L. Liang, X. H. Lu, Y. X. Tong, **Vanadium nitride nanowire supported SnS₂ nanosheets with high reversible capacity as Anode material for Lithium ion batteries** ACS Appl. Mater. Interfaces, 7 (2015), pp. 23205-23215
- [28] L. Xin, X. H. Sun, Z. W. Gao, X. D. Hu, L. Rui, C. Shu, C. M. Zheng, W. B. Hu **A Simple one-pot strategy for synthesizing ultrafine SnS₂ nanoparticle/graphene composites as anodes for lithium/sodium-ion batteries** ChemSusChem, 11 (2018), pp. 1549-1557
- [29] J. T. Zai, K. X. Wang, Y. Z. Su, X. F. Qian, J. S. Chen **High stability and superior rate capability of three-dimensional hierarchical SnS₂ microspheres as anode material in lithium ion batteries** J. Power Sources, 196 (2011), pp. 3650-3654

- [30] J. Xia, L. J. Liu, J. J. Xie, H. X. Yan, Y. T. Yuan, M. F. Chen, C. Huang, Y. Zhang, S. Nie, X. Y. Wang, **Layer-by-layered SnS₂/graphene hybrid nanosheets via ball-milling as promising anode materials for lithium ion batteries** *Electrochim. Acta*, 269 (2018), pp. 452-461
- [31] X. Chen, H. Jiang, Y. X. Pei, Y. L. Chen, Y. B. Zeng, H. Guo **Binder-free ultrathin SnS₂ with superior reversibility of conversion reaction for high-rate lithium ion batteries** *J. Alloys Compd.*, 873 (2021), p. 159623
- [32] W. Wei, F. F. Jia, K. F. Wang, P. Qu **SnS₂/graphene nanocomposite: A high rate anode material for lithium ion battery** *Chin. Chem. Lett.*, 28 (2017), pp. 324-328
- [33] Q. Wang, Y. X. Nie, B. He, L. L. Xing, X. Y. Xue **SnS₂-graphene nanocomposites as anodes of lithium-ion batteries** *Solid State Sci.*, 31 (2014), pp. 81-84,
- [34] J. P. Li, P. Wu, F. J. Lou, P. Zhang, Y. W. Tang, Y. M. Zhou, T. H. Lu **Mesoporous carbon anchored with SnS₂ nanosheets as an advanced anode for lithium-ion batteries** *Electrochim. Acta*, 111 (2013), pp. 862-868
- [35] J. F. Yin, H. Q. Cao, Z. F. Zhou, J. X. Zhang, M. Z. Qu **SnS₂@reduced graphene oxide nanocomposites as anode materials with high capacity for rechargeable lithium ion batteries** *J. Mater. Chem.*, 22 (2012), pp. 23963-23970
- [36] Y. D. Ren, W. M. Lv, F. S. Wen, J. Y. Xiang, Z. Y. Liu **Microwave synthesis of SnS₂ nanoflakes anchored graphene foam for flexible lithium-ion battery anodes with long cycling life** *Mater. Lett.*, 174 (2016), pp. 24-27
- [37] P. Wang, M. Q. Shen, H. Zhou, C. F. Meng, A. H. Yuan **MOF-derived CuS@Cu-BTC composites as high-performance anodes for Lithium-ion batteries** *Small*, 15 (2019), p. 1903522
- [38] L. X. Yin, H. M. Li, R. L. Cheng, J. Yang, X. G. Kong, J. F. Huang, X. Wang **Controllable synthesis of SnS₂ nanoflakes as high-performance anode for lithium-ion batteries** *J. Mater. Sci. Mater. Electron.*, 32 (2021), pp. 191-203,
- [39] Y. Y. Wang, J. H. Zhou, J. H. Wu, F. J. Chen, P. R. Li, N. Han, W. J. Huang, Y. P. Liu, H. L. Ye, F. P. Zhao, Y. G. Li **Engineering SnS₂ nanosheet assemblies for enhanced electrochemical lithium and sodium ion storage** *J. Mater. Chem. A*, 5 (2017), pp. 25618-25624
- [40] X. R. Shi, Z. Y. Zhou, J. P. Yin, S. Li, S. J. Ji, J. C. Sun, Z. S. Wen **Fabrication of rGO/g-C₃N₄@SnS₂ and its rate-performance enhancement** *Chem. Phys. Lett.*, 746 (2020), p. 137296
- [41] H. T. Huu, H. T. T. Le, T. H. Nguyen, N. L. Thi, V. Vo, W. B. Im **Facile synthesis of SnS₂@g-C₃N₄ composites as high performance anodes for lithium ion batteries** *Appl. Surf. Sci.*, 549 (2021), p. 149312